

Room-Temperature Annealing-Free Gold Printing via Anion-Assisted Photochemical Deposition

Dong Wu, Bowen Yao, Shuwang Wu, Hardik Hingorani, Qingyu Cui, Mutian Hua, Imri Frenkel, Yingjie Du, Tzung K. Hsiai, and Ximin He*

Metal patterning via additive manufacturing has been phasing-in to broad applications in many medical, electronics, aerospace, and automotive industries. While previous efforts have produced various promising metal-patterning strategies, their complexity and high cost have limited their practical application in rapid production and prototyping. Herein, a one-step gold printing technique based on anion-assisted photochemical deposition (APD), which can directly print highly conductive gold patterns ($1.08 \times 10^7 \text{ S m}^{-1}$) under ambient conditions without post-annealing treatment, is introduced. Uniquely, the APD uses specific ion effects with projection lithography to pattern Au nanoparticles and simultaneously sinter them into tunable porous gold structures. The significant influence of kosmotropic or chaotropic anions in the precursor ink on tuning the morphologies and conductivities of the printed patterns by employing a series of different ions, including Cl^- ions, in the printing process is presented. Additionally, the resistance stabilities and the electrochemical properties of the APD-printed gold patterns are carefully investigated. The high conductivity and excellent conformability of the printed Au electrodes are demonstrated with reliable performance in electrophysiological signal delivery and acquisition for biomedical applications. This work exploits the potential of photochemical-deposition-based metal patterning in flexible electronic manufacturing.

“lift-off” technique by conventional photolithography. Such subtractive manufacturing methods, due to their long cycle time, strict operation conditions and complex procedures, have been phased-out in industrial rapid production and prototyping facilities.^[5]

With the rapid advancement of contemporary additive manufacturing techniques, the aforementioned issues have been partially remedied by inkjet printing and direct laser writing (DLW).^[6] Inkjet printing has been utilized to readily print silver particle/nanowire composites,^[7–11] but it requires careful optimization of the precursor’s rheological properties to achieve printability, and then a post-treatment to enhance the necessary conductivity.^[12,13] DLW has been used to print silver via a photochemical process, where metal ions are photoreduced from metallic salt solutions within selective voxels to form metal patterns and structures.^[14,15] This emerging technique has substantially extended the resolution in fabrication to micro- and sub-microlevels. Delicate 2D or 3D metal, or metal-polymer composite

structures with a feature size of 120 nm can be fabricated via multiphoton-induced reactions.^[16–18] Nonetheless, DLW suffers from low efficiency when printing millimeter-scale patterns or structures.^[19]


Particularly, Digital Light Processing (DLP)-based projection lithography for metal printing has been developed to fill this gap, in which planar patterns are printed in parallel instead of in series.^[20–22] Applying DLP to metal printing can significantly simplify metal-patterning processes for either subtractive or additive manufacturing.^[23,24] Previously, we reported a room-temperature printing method using visible light. Highly conductive, patterned silver could be produced after a simple chemical annealing process of as-printed patterns.^[25] A similar printing process utilizing a blue laser sintering post-treatment was also reported.^[26] Functional polymers have been utilized to assist electroless deposition of metal thin films and patterns, and a similar strategy was applied to DLP-based metal printing recently.^[27] Recently, Zhao et al. proposed to use a polymer backbone to guide the growth of metal particles to achieve a dense metallic thin film, which eliminates the need for post-treatment.^[28] Despite the progress achieved, issues and

1. Introduction

Advancements in metal-patterning technologies have improved the miniaturization, cost-efficiency, productivity and customization of a variety of applications including integrated circuits, micro-optical components, micro electromechanical systems, wearable electronics and biosensing devices.^[1–4] Metal patterning is commonly realized through selective etching or

D. Wu, B. Yao, S. Wu, H. Hingorani, M. Hua, I. Frenkel, Y. Du, X. He
Department of Materials Science and Engineering
University of California
Los Angeles (UCLA), Los Angeles, CA 90095, USA
E-mail: ximinhe@gmail.com

Q. Cui, T. K. Hsiai
Department of Bioengineering
University of California
Los Angeles (UCLA), Los Angeles, CA 90095, USA

 The ORCID identification number(s) for the author(s) of this article can be found under <https://doi.org/10.1002/adma.202201772>.

DOI: 10.1002/adma.202201772

challenges such as limited thickness, singularity of structures, the short lifetime of inks and a lack of investigations into electrochemical properties and applications, necessitates additional studies of this metal-patterning approach. Furthermore, silver is the focus of most published works, while gold, a noble metal with extraordinary chemical stability, conductivity, optical properties, catalytic capability and biocompatibility, has not yet been systematically studied in DLP-based metal printing.

Thus, we present a simple and novel strategy for one-step annealing-free metal patterning, namely anion-assisted photochemical deposition (APD). APD utilizes specific ion effects with projection lithography to directly print high conductivity ($1.08 \times 10^7 \text{ S m}^{-1}$, 24% of the bulk Au conductivity) gold patterns by simply projecting digital images on either rigid or flexible substrates at ambient conditions. The specific ion effect, also known as the Hofmeister effect, describes the changes of protein solubility induced by salts with varied ionic strength. By appropriately increasing the ionic strength of a solution, the solubility of a protein can be increased—referred to as “salting in”—while with a very high ionic strength, a protein solute can be precipitated—referred to as “salting out”. In recent decades, this concept has been extended to many other macromolecules and broad researching fields such as hydrogels, nucleation, and self-assembly.^[29–31] It has found its way into metallic nanotechnology as well, specifically so in laser synthesis and processing of colloids.^[32] Moreover, Du et al. succeeded in fabricating noble metal aerogels by taking advantage of specific ion effects.^[33] In this work, we propose an APD technique which utilizes specific ion effects to assist the direct deposition and growth of gold nanoparticles (AuNPs) networks, and in doing so, APD allows us to achieve tunable porous gold structures. Such controllability over gold’s morphologies offers great potential for broader applications where a variance in nano- and/or microstructure is demanded. In addition, conformable gold electrodes are printed to demonstrate such potential in the exemplary context of electrophysiological signal delivery and acquisition.

2. Results and Discussion

2.1. Process and Principle of Au Printing

A DLP-based projecting system with 385 nm ultraviolet (UV) light source was employed to achieve the metallic gold patterning (Figure 1a). Digital images were projected on the interface between the precursor ink and the transparent substrates. A typical ink consists of chloroauric acid (HAuCl_4 , 48 g L^{-1}) as the gold source, photoinitiator lithium phenyl-2,4,6-trimethylbenzoylphosphine (TPO-Li, 0.6 g L^{-1}) to generate free radicals for reduction reaction, and sodium chloride (NaCl , 20 g L^{-1}) as a printing-aid agent. This ink allows us to directly print Au patterns on either rigid or flexible substrates with a positively charged polymer coating (Figure 1b).

We investigated the APD process with the typical gold precursor ink and proposed the printing principle (Figure 1c). Within 5 min of projection, a layer of loosely distributed AuNPs can be observed deposited onto the substrate (Figure 2a,d). Most of the AuNPs were $\approx 60 \text{ nm}$ in diameter. Adjacent AuNPs attached to each other forming an AuNP network with a

porosity of 12% (Figure 2i). However, the sharp and clear outlines of the AuNPs indicated that only a limited amount of AuNPs were fused together to allow electrical current to flow through. Lacking in long-range, continuous, conductive paths, this printed Au pattern was non-conductive. As the deposition proceeded to 10 min, the conductivity of the printed pattern drastically increased to $3.6 \times 10^6 \text{ S m}^{-1}$, due to an abundant formation of conductive paths. This was confirmed by scanning electron microscope (SEM) imaging (Figure 2b,e), which also showed the growth of AuNPs (Figure S1, Supporting Information). Despite the vacant regions between AuNPs seem to expand in the SEM image, the total porosity of the AuNPs network decreased to $\approx 9\%$. We believe this can be attributed to the recrystallization of small AuNPs. Small and unstable nuclei below the critical nucleation radius would eventually be consumed to form conductive paths while the others would grow larger. As the printing continued to 20 min, we can obtain a dense and continuous AuNPs layer with a higher conductivity of $6.4 \times 10^6 \text{ S m}^{-1}$. The porosity of the network dropped to $\approx 2\%$ and remained stable even with further illumination. The densification process of the Au pattern was also reflected by the rapid increase of its optical reflectance and the decrease of light transmittance throughout the printing process (Figure S2, Supporting Information). Although the irregular shape of AuNPs can still be observed, the edges of the AuNPs have become obscure (Figure 2c,f). Given previous work has concluded the specific ion effect induces destabilization and gel formation in metal nanoparticles solutions,^[33] we believe that the presence of Cl^- ions in our procedure promoted in situ fusion between the newly generated AuNPs and subsequently deposited AuNPs thus filling the initially observed gaps within this short period of time (Figure 2e,f).

In addition, the thickness variation of the printed Au was also studied during the printing process of the typical ink (Figure 2g). The growth rate of the thickness was relatively slow within the first 5 min (3.1 nm min^{-1}). Once a layer of separated AuNPs is formed, the deposition rate rapidly increased (5.6 nm min^{-1}) and an Au pattern over 100 nm thickness was obtained in 30 min of printing. It was observed that the growth rate (the slope of the thickness–printing-time curve) slowly decreased after 15 min of printing, which we attributed to the decline in the number of available photons for the reaction. This was validated by the rapid decrease of transmittance of the printed Au pattern at 385 nm during the printing process (Figure S2b, Supporting Information). After 30 min, we observed the transmittance dropped to below 2% as a dense pattern formed in the path of the UV light source located below the sample, hindering further deposition from taking place above. The decline of available photons as the printing proceeded could be attributed to the printing setup, in which the UV exposure occurred from the backside of substrates. If UV patterns are projected from above, some AuNPs can be generated via homogeneous nucleation forming suspension and scattering the light, which eventually leads to unsuccessful patterning. Challenges are expected to be addressed in controlling the kinetics of the photoreduction reaction to confine it to the liquid–solid interface. By optimizing the ink recipe, top-down DLP printer with light projected from above substrates

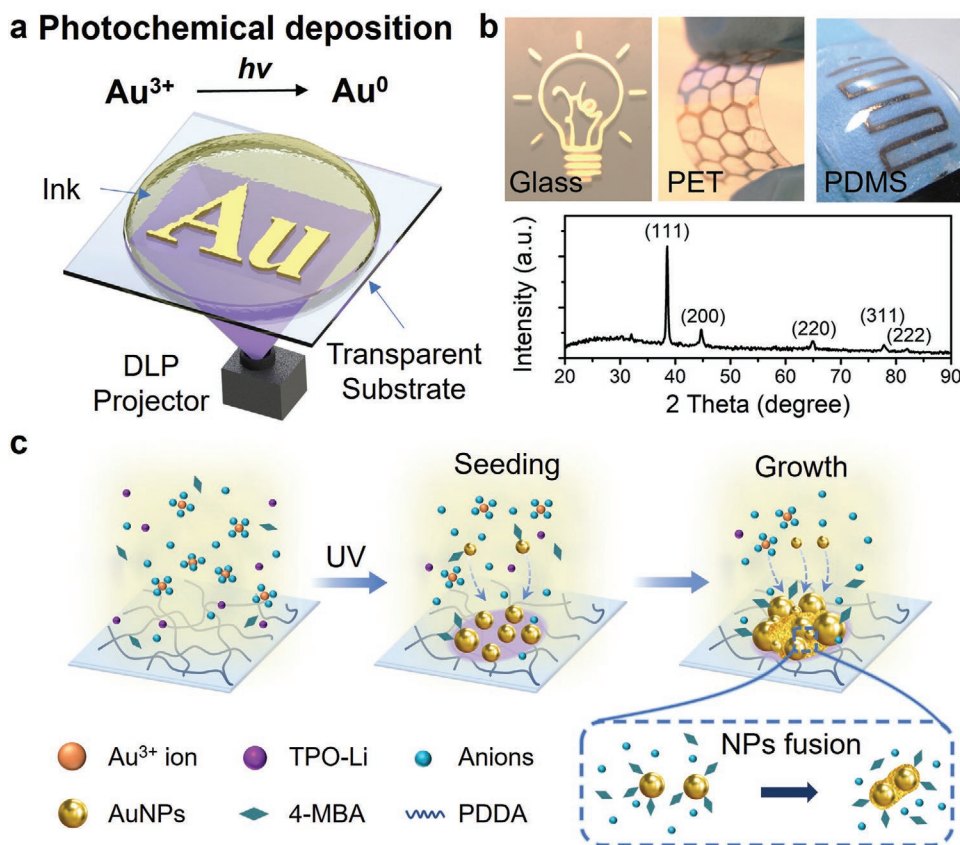


Figure 1. a) Schematic of the DLP-based printing setup. b) The printed patterns on different substrates (top) and XRD spectrum of printed gold (bottom). c) Principle of the printing involving the reduction of gold ions, the seeding of AuNPs, and the growth of AuNPs network (top). The zoom-in AuNPs fusion occurs during the growth process (bottom).

can replace the current bottom-up system, which endows broader applications for the APD method.

The APD printing involved three different processes: reduction of gold ions, seeding of AuNPs, and anion-assisted growth of AuNPs network (Figure 1c). As the ink was placed on the substrate, no reaction would occur until a UV light pattern was projected on the interface between the substrate and ink. Upon UV photon flux, radicals were in situ generated through the cleavage of the Norrish type I photoinitiator, TPO-Li, to reduce Au^{3+} to Au^0 .^[34] This photon-induced reduction proceeded until the light was blocked by the deposited layer as mentioned above. The produced Au^0 aggregated into AuNPs and 4-mercaptobenzoic acid (4-MBA) attached to the surface of AuNPs via thiol-gold bonding. 4-MBA can help stabilize the AuNPs and restrict their growth.^[35–37] A limited quantity of 4-MBA was used in the ink to obtain AuNPs with appropriate sizes to serve as the foundation, upon which further growth and subsequent in situ fusion of AuNPs occurred. Meanwhile, Cl^- ions were adsorbed onto the AuNPs due to the electrostatic force, making them negatively charged on their surfaces. Once the AuNPs formed, they would then undergo the seeding process. To anchor the AuNPs, the substrate was coated with a polymeric layer of high positive-charge density, specifically poly(diallyldimethylammonium chloride) (PDDA). The PDDA coating on the substrate is essential for printing, in the absence of which complete Au patterns can hardly be deposited on

substrates (Figure S7c, Supporting Information). Two driving forces that caused the aggregated AuNPs to deposit onto the substrate were settlement driven by gravity and the electrostatic attraction between the AuNPs and the polymer coating, where the latter was more dominant. As the small AuNPs were deposited on the substrate, they acted as seeds for further growth. This seeding process is reflected in the observation of a relatively slow deposition rate during the first 5 min of the printing process, which is kinetics-dominated. After that, the deposited AuNPs grew larger (Figure 2d and Figure S1, Supporting Information), and new smaller AuNPs formed (Figure 2f) due to the incessant reduction of Au^{3+} to Au^0 . In conclusion, we suggest that the synergistic effect of the growth of AuNPs and the filling of newly formed ones densified the AuNP network. Anions, like Cl^- ions, then played a significant role in achieving a conductive path between the neighboring AuNPs. Specifically, the presence of anions altered the aqueous environment surrounding the AuNPs. The strongly hydrated kosmotropic anions, like Cl^- , were rather repelled from the interface between the AuNPs and the solution, resulting in greater surface energy on the AuNPs.^[32,33] This drove fusion as the uncapped AuNPs approach each other, to form conductive paths and eventually develop into a conductive AuNP network via repeating the process above.

The flux of UV photons controlled by the projector also significantly affected the thickness of the Au pattern (Figure S3,

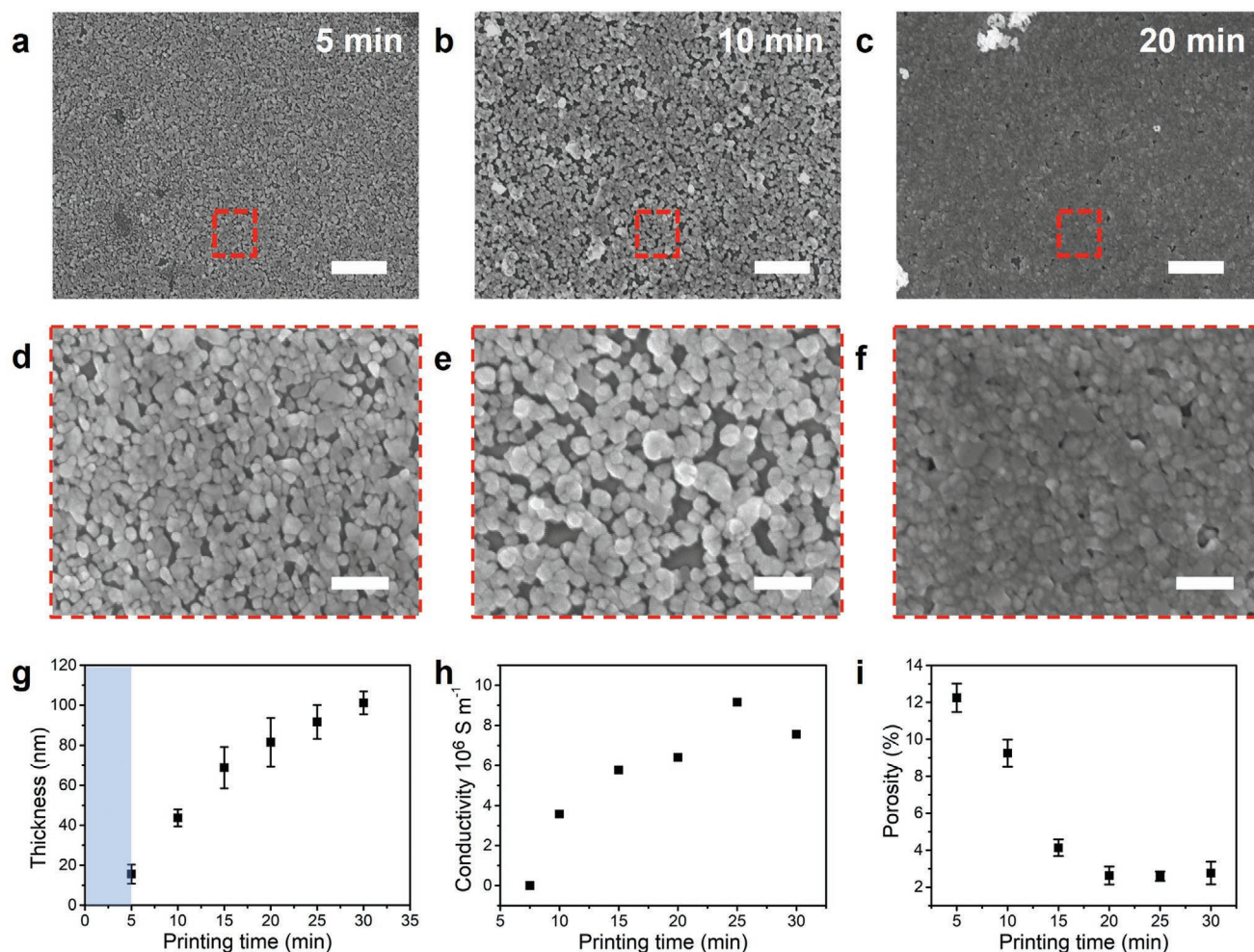


Figure 2. a–c) SEM images of the printed gold with illumination time of 5, 10, and 20 min. d–f) Zoom-in microstructures of the printed gold. g) Thickness of printed gold patterns as a function of printing time. h) Conductivity of printed gold patterns as a function of printing time. i) Porosities of printed gold patterns as a function of printing time. Data represent mean \pm standard deviation, $n = 5$, significance determined by one-way ANOVA test. Scale bars: $1 \mu\text{m}$ for (a–c), 300 nm for (d–f).

Supporting Information). An increase in light intensity can lead to the formation of a thicker Au layer. The properties of the printed Au pattern were not only determined by the illumination time and the intensity of light source, but also significantly depended on the chemical composition of the precursor inks. We investigated the influence of pH values on the precursor. Different traces of sodium hydroxide solution were added into the original, unaltered precursor to tune the pH values of the inks (Figures S4 and S5, and Table S1, Supporting Information). The pH value of the original precursor ink was 2.13, conditions under which TPO-Li accepted protons, becoming less hydrophilic, and causing it to precipitate. Even though the photoinitiated reduction can still occur, the resultant white precipitant scattered light and acted as nucleation sites, which lead to inaccurately patterned printing. If the pH value is tuned to be above 7, TPO-Li becomes unstable and directly reduced Au^{3+} into Au^0 without any luminous energy input. The ink was colorless as prepared, but at this pH a dark violet AuNPs suspension formed in minutes. Additionally, black Au foam

eventually formed due to the presence of Cl^- salt when the alkaline precursor was allowed to sit undisturbed for at least 6 h (Figures S5d and S6, Supporting Information). This observation was previously noted in works pertaining to a metal foam synthesis, further demonstrating the important role of anions in our printing strategy.^[33] Therefore, we conclude that the stability of the ink is determined by the behavior of TPO-Li under different pH conditions. The ideal pH value for the precursor was validated to be ≈ 6 . Under this condition, there was no formation of either the TPO-Li precipitant or AuNPs, and the precursor ink still functioned properly succeeding 48 h of storage in the dark and at room temperature.

2.2. Specific Ion Effects on the Printed Au Patterns

We investigated the properties of the Au patterns printed for 20 min with varied NaCl concentrations to further demonstrate the significance of the Cl^- in the APD process. Without

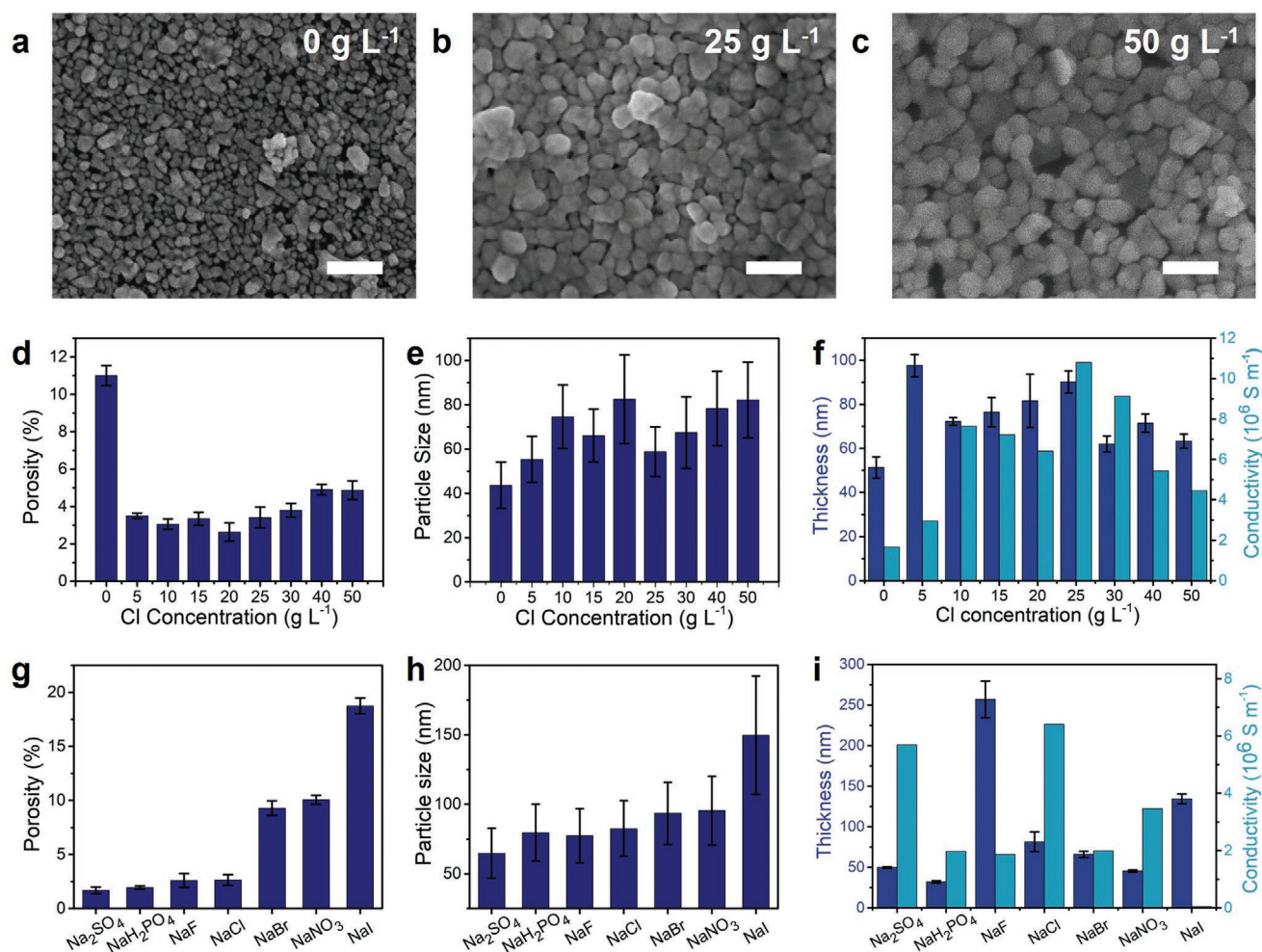


Figure 3. a–c) SEM image of printed Au using inks with NaCl concentrations of 0, 25, and 50 g L⁻¹ respectively. d) Porosity as a function of Cl⁻ anion concentrations. e) Particle sizes as a function of Cl⁻ anion concentrations. f) Thickness and conductivity as a function of Cl⁻ anion concentrations. g) Porosity of samples with different anions. h) Particle sizes of samples with different anions. i) Thickness/conductivity of samples with different anions. Data represent mean ± standard deviation, *n* = 5, significance determined by one-way ANOVA test. Scale bar: 200 nm for (a–c).

additional sodium salts, a loosely arranged network with a porosity of 11% was deposited on the substrates. (Figure 3a) The deposited Au pattern was ≈51 nm thick, while the measured conductivity was $1.67 \times 10^6 \text{ S m}^{-1}$. Even though large gaps can be observed among AuNPs, conductive pathways can still form due to the limited amount of Cl⁻ in the HAuCl₄ stock solution. As the NaCl concentration was increased to 25 g L⁻¹, a thicker pattern (≈81 nm) with a higher density (porosity of 3.4%) of larger AuNPs of 59 nm in length was printed (Figure 3b). As mentioned above, Cl⁻, as a kosmotropic ion, can stabilize the water–water interactions surrounding AuNPs and lower the surface energy. This allowed the AuNPs to grow and sinter together to form more conductive pathways, which consequently raised the conductivity to $1.08 \times 10^7 \text{ S m}^{-1}$. Such a high conductivity is comparable to those obtained by inkjet printing, which however requires high temperature annealing (Table S4, Supporting Information). As we continued to increase the concentration to 50 g L⁻¹, both conductivity and thickness decreased while the porosity increased slightly to 4.9%. We believe that the high Cl⁻ concentration made the AuNPs more negatively charged,

leading to greater repulsion between AuNPs due to electrostatic forces, which ultimately prevented the AuNPs from sintering (Figure 3c). As a result, fewer conductive pathways could form, compared to using an ink with moderate concentrations of NaCl. In general, we suggest that Cl⁻ can lower the surface energy of AuNPs promoting their sintering and growth at moderate concentration. It can also stabilize the AuNPs by blocking active sites and forming electrostatic repulsion between them. The synergistic effect of both processes eventually led to the porosity change with varied Cl⁻ concentrations (Figure 3d).

Other sodium salts at equal concentrations were utilized in various precursor inks to investigate the influence of these different anions on gold printing via APD. The porosities (Figure 3g), the particle size (Figure 3h), and the microstructures (Figure S9, Supporting Information) were shown to trend with salt variation that expectedly corresponds to the Hofmeister series: Na₂SO₄ > NaH₂PO₄ > NaF > NaCl > NaBr > NaNO₃ > NaI. Printed Au with high density and small particles can be achieved with the presence of kosmotropic SO₄²⁻ anions, while a loose network with much larger AuNPs can be obtained

through the addition of chaotropic I^- ions. Continuous and more packed AuNPs networks form with the presence of an ionic kosmotrope. These kosmotropic anions can be utilized to lower the surface energy of AuNPs, promote their growth and sinter the AuNPs. On the other hand, the chaotropic ions tended to be adsorbed onto the surface of AuNPs, leading to the repulsion of negatively charged AuNPs. Thus, AuNPs were loosely distributed on the substrate and conductive paths are barely formed. Despite the great correlation between the structures and anions, the thickness and conductivity of the printed Au were not closely related to the Hofmeister series (Figure 3i and Table S2, Supporting Information). The thickness and conductivity involved more complex kinetics and thermodynamic processes during the printing. Multiple factors including, but not limited to, crystalline structures, particle sizes, deposition rate, sintering of AuNPs, interaction between Au ions and anions, and the possible formation of Au^+ ions can contribute to the final performance of the deposited Au. Even though there are still challenges to fully understand the deposition process, tunable porous structures of Au patterns can be achieved via APD, which is significant for fulfilling broad applications in electronic industries such as electrode fabrication and flip chip packaging. Therefore, we plan to conduct more fundamental studies on the deposition process in the future.

2.3. Electrical Performance of the Printed Au Patterns

We demonstrated that our APD method can be conducted on both rigid and flexible substrate (Figures 1b and 4a). Au

patterns on both glass and PDMS substrates were incorporated into circuits to power light-emitting diodes (LEDs). The long-term stability of electrical performance was verified by measuring the resistance change in ambient condition. No obvious degradation in the conductivity of the pattern was observed (Figure S22a, Supporting Information). At the same time, we also looked at the resistance variation of the printed Au pattern on a soft PDMS substrate under bending and stretching. Au strip patterns were printed with the typical ink onto a flexible PDDA-coated PDMS thin film. Changes in resistance due to different bending radii during inward and outward bending were measured respectively (Figure 4b). By bending the pattern outward at a radius anywhere from 24 mm down to 8 mm, the change in resistance was negligible given the ductility of gold network. As the bending radius decreased further, however, the resistance rapidly increased due to the breakdown of conductive paths under localized stretching (R/R_0 increased from 1.22 to 4.62). Alternatively, the resistance reduced as the sample was bent inward. Compressive strain enhanced the packing density of the AuNPs, creating more conductive paths through the networks. As the inward bending radius decreased to 4 mm, the resistance of the gold network dropped to less than half. Once the printed gold returned to its original flat state, the resistance also restored. In addition to the bending tests, the printed Au strip patterns were stretched under different strains ranging from 0% to 50% (Figure 4c). As the strain increased, the resistance of the Au pattern also increased proportionally, making it possible to function as a strain sensor. As the strain rose to over 50%, the printed Au pattern became non-conductive. The SEM images show that

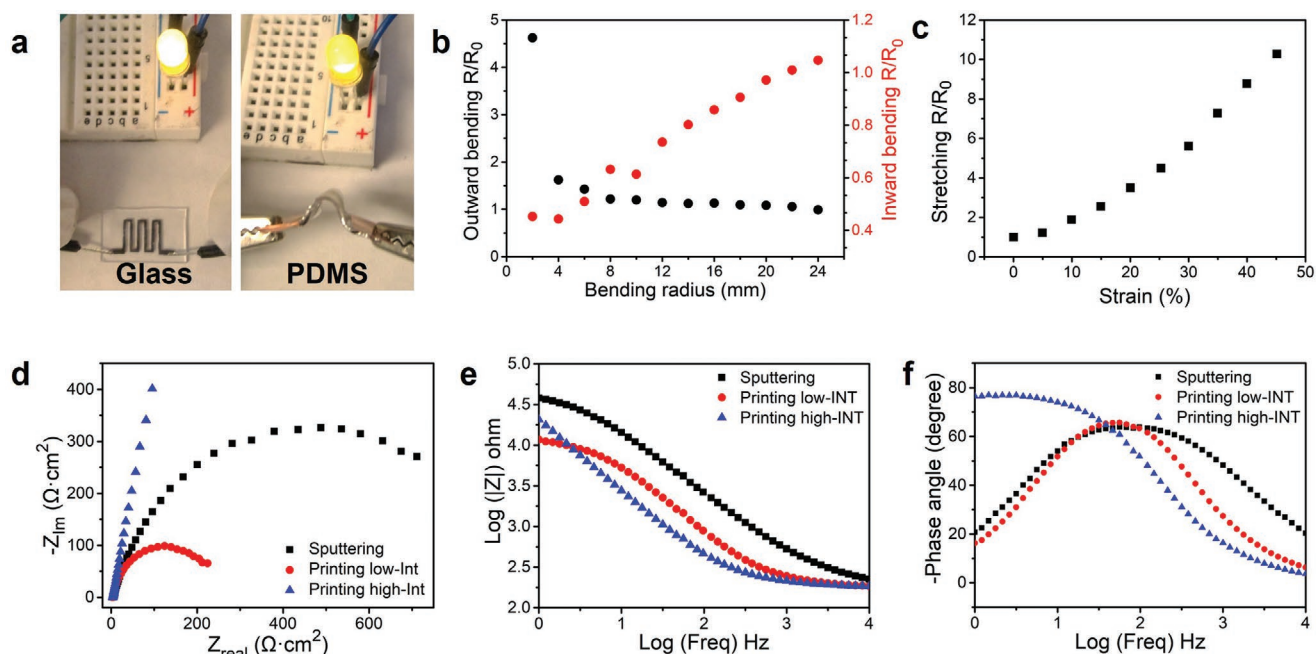


Figure 4. a) Au circuit printed on rigid and flexible substrate connected with a LED light. b) Resistance stability of printed flexible Au electrode on PDMS substrate under inward and outward bending. c) Resistance stability of printed flexible Au electrode on PDMS substrate under stretching. d–f) Electrochemical impedance spectra (EIS) within a frequency range of $1-10^4$ Hz with an amplitude of 5 mV of sputtered gold and printed gold electrodes with different light intensity: d) Nyquist plots for the gold electrodes. e) Bode plots for the gold electrodes: impedance as a function of frequency. f) Bode plots for the gold electrodes: phase angle as a function of frequency.

the printed Au pattern was an intact and connected layer before stretching at 50% strain (Figure S13a, Supporting Information), while it broke into many small rectangular fragments after the stretching (Figure S13b, Supporting Information). It is worth noting, even with the formation of cracks on the printed Au pattern under 50% strain, the pattern still partially restored its conductivity upon release. The resistance stability of the printed Au pattern was tested by stretching the sample to 50% strain 1000 times (Figure S14, Supporting Information). The resistances were measured after a stretching cycle ended. The results showed that during the first three cycles, the resistance had almost no change due to the intrinsic ductility of gold. After that, the resistance increased and eventually stabilized at around twice the original value. Under multiple cycles of stretching, the printed Au layer broke down into fragments in order to release the stress, while some portions remained connected and formed conductive paths. Therefore, the Au patterns can reach a newfound stability with high conductivity under small strain.

2.4. Tunable Electrochemical Performance

Due to the tunability of the properties and morphologies of the printed gold patterns, we suggest porosity of the gold networks may contribute to their electrochemical performance as electrodes. Therefore, we investigated the impedance performance of the printed gold electrodes. Three porous Au electrodes with similar thicknesses were prepared by printing with a low ($\approx 3 \text{ mW cm}^{-2}$) and high intensity ($\approx 5 \text{ mW cm}^{-2}$), and sputtering. Both the printed Au electrodes showed comparable or lower impedance than the sputtered one, validating the potential for application as electrodes in electrochemical reaction systems (Figure 4e). For the electrodes printed with low intensity (low-Int electrodes), the structure was more porous. In Nyquist plots (Figure 4d), the smaller semicircle of the low-Int electrodes indicated its smaller charge transfer resistance (R_2 in Figure S16, Supporting Information) compared to the sputtered electrodes. In brief, the low-Int electrodes showed higher electrocatalytic capability and may benefit applications like electrocatalysis and electrochemical sensing. For the electrodes printed with high intensity (high-Int electrodes), the structure was denser. In Nyquist plots (Figure 4d), no semicircle was observed for the high-Int electrodes, which indicated the active sites were blunted and electrochemical reactions were suppressed. This was also reflected in the increase of phase angles to around -80° at low frequency in Bode plots (Figure 4f). Therefore, the high-Int electrodes can provide stable transduction between electrons and ions at the same time with a lower impedance than the sputtered Au, which partially remedied the conflicts between low impedance and the high stability of porous Au electrodes. In conclusion, the tunability achieved by APD allows us to adjust the electrochemical performance of the printed electrodes to meet the requirements of different applications such as electrocatalysis and electrophysical signal transmission with low impedance at the same time. This offers more significance of the Au electrodes fabricated via APD in future studies.

2.5. Printed Au Electrodes for Electrophysiology Signal Delivery and Acquisition

To demonstrate the excellent conductivity, flexibility, conformability and light weight of the gold electrode that we fabricated here, several biological applications involving electrophysiology signal delivery and acquisition were conducted. First, two soft electrodes were fabricated by printing Au films on two flexible poly(ethylene terephthalate) (PET) thin films separately, and they can be conformally attached to the epicardium of the right ventricles of a porcine heart after euthanasia of the test subject (Figure 5a). To externally pace the heart with the printed Au electrodes, an electrical pulse at a condition commonly used for commercial gold electrodes was applied, specifically with an amplitude of 2–3 V, a pulse width of 1 ms and a pacing rate of 60 beats per minute. As shown by Movie S1, Supporting Information, the porcine heart was successfully paced, which exhibited an excellent charge delivery capability of the printed Au electrodes. Additionally, we took advantage of the printability by fabricating a pair of Au electrodes on a single PET thin film with a single exposure, and then conformally attached them to the small and soft lobes of a Venus flytrap by introducing a thin hydrogel as an adhesive layer (Figure 5b). The Venus flytrap can be modulated quickly from an “open” to a “close” state in less than 6 s through the compliant electrodes acting on a square-wave alternating voltage of 3 V, similar to the gold nanomesh electrodes reported previously (Figure 5b and Movie S2, Supporting Information).^[38] Such a patterning ability via APD allows for the fast and facile fabrication of multiple electrodes on one substrate with a single exposure, which may benefit complex biological modulation in future. Not only performing electrical stimulation (injecting electrons), the printed Au electrodes can be also used for recording (collecting electrons), owing to their high conductivity and conformability. The action potential during the flytrap’s open-to-close actuation of a large deformation and curvature change was successfully recorded without an amplifier (Figure 5c). This indicates its excellent ability of acquiring electrical signals with a high signal-to-noise ratio.

To further investigate the conformal Au electrodes’ ability to collect complex signals, electrocardiogram (ECG), electromyography (EMG), and electroencephalography (EEG) signals were acquired (Figure 5e,g). In the ECG tests, the printed Au electrodes and Ag/AgCl electrodes (as control) were attached to the fingers of a volunteer. The ECG signals were recorded for 10 s and the signals from a single beat were extracted from the data (Figure 5e). The P wave, QRS complex, and T wave were clearly observed in the ECG signals collected using printed Au electrodes. The total QRS wave amplitude of the signals collected by the printed Au electrodes was 0.684 mV, comparable to the one collected by Ag/AgCl electrode (0.868 mV). ECG signals were also recorded right after the volunteer’s engagement in squat exercises, showing the heart rate increased from 66 bpm to 102 bpm (Figure S17, Supporting Information). The signals were recorded for 5 min to highlight the reliability and stability of the printed gold electrodes (Figure S18, Supporting Information). The application of the printed Au electrodes was also demonstrated in EMG and EEG tests. Four electrodes were attached to the forehead, the back of the head, and both the earlobes of

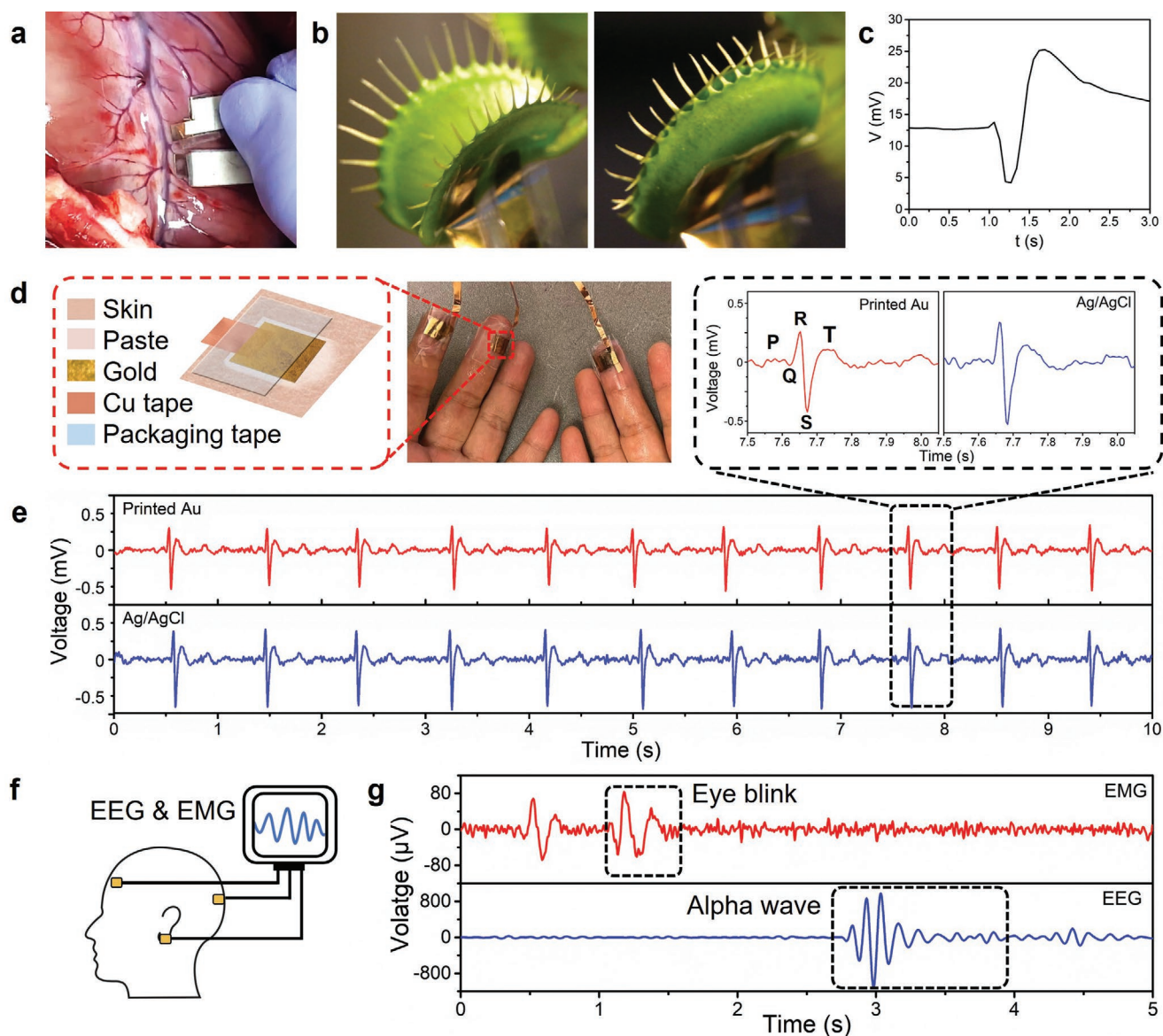


Figure 5. Conformable printed Au electrodes in electrophysiological signal delivery and acquisition. a) A pair of Au electrodes attached to the epicardium of the right ventricles for the porcine heart pacing with an electrical pulse. b) A pair of Au electrodes attached to the lower epidermis of a Venus flytrap lobe to modulate the lobe shift from “open” (left) to “close” (right) state with a square wave electrical stimulation. c) Action potential of the Venus flytrap actuator measured by the printed Au electrodes. d) The laminate structure diagram and optical image of the printed Au electrodes for ECG test. e) Pulse signal recording (10 s) and sample of a single beat (top), obtained by printed Au electrodes (red) and Ag/AgCl (blue) electrodes. f) Schematic of EMG and EEG test. g) EMG and EEG signal recordings during eye blink.

the human subject separately (Figure 5f). The EMG and EEG signals were recorded for 5 s, featuring the two eye blinks of the test subject. After the eyes of the test subject closed for ≈ 1 s, an alpha wave signal was detected (Figure 5g). These results suggested that the printed Au electrodes can be safely and reliably used for electrophysiological signal delivery and acquisition.

3. Conclusion

We have demonstrated a facile direct patterning strategy to produce highly conductive metallic gold on various substrates

under ambient conditions via APD. This approach combines projection lithography with specific ion effects to achieve a one-time patterning of gold without post annealing treatment, which simplifies the fabrication process of metal patterning by improving both its time- and cost-efficiency. The typical printing process was investigated carefully, and a model involving three processes was proposed to understand the principle of APD. Our results showed substantial tunability in the structures, electrical properties, and electrochemical performance of the printed gold. We further demonstrated the high conductivity ($\approx 10^7$ S m^{-1}) and conformability of the Au electrodes fabricated by our method via effective electrophysiological signal

delivery and acquisition. With the satisfactory performance of the conformal Au electrodes printed in this work, we expect the APD method to continue to be explored and that it will find far-reaching applications throughout wearable electronics, soft robotics, biochemical sensing and electrochemistry.

4. Experimental Section

Materials: Chloroauric acid (HAuCl_4), 4-mercaptobenzoic acid (4-MBA), sodium chloride, sodium hydroxide, sodium phosphate monobasic, sodium nitrate, sodium sulfate, sodium bromide, sodium iodide poly(diallyldimethylammonium chloride) solution (PDDA), PET thin film, Sylgard-184 silicone elastomer (PDMS), acrylic acid (AAc) and phosphate buffered saline (PBS) solution were purchased from Sigma-Aldrich, Inc. Ethanol was purchased from Fisher Scientifics, Inc. Ten20 conductive paste and Ag/AgCl electrodes were purchased from OpenBCI, Inc. Lithium phenyl-2,4,6-trimethylbenzoylphosphinate (TPO-Li) was purchased from Arkema Inc. All chemicals were used without further treatment.

Ink Formulation: Stock solutions with different components were prepared separately: 6 mg mL⁻¹ TPO-Li aqueous solution, 60 mg mL⁻¹ HAuCl_4 aqueous solution, 10 mg mL⁻¹ 4-MBA ethanol solution, 100 mg mL⁻¹ NaOH aqueous and DI water. The printable gold inks in this work were formulated by mixing the as prepared stock solutions of TPO-Li, HAuCl_4 , DI water, 4-MBA and NaOH in the volume ratios of 1:0.125:0.125:0.015:0.015. Then certain amount of sodium salts was added and mixed under vortex to form the printing ink with specific anions.

Substrate Treatment: Substrates were coated with PDDA to assist the seeding process of AuNPs. Glass and PDMS substrates were first rinsed with 2-propanol, DI water and ethanol under ultrasonication in sequence, then dried with air. Only water rinsing was conducted on PET substrate to avoid the damage from the organic solvent. The substrates were then subjected to oxygen plasma treatment to make the surface reactive and immersed in a 0.1 M PDDA aqueous solution for 1 h. Eventually, the coated substrates were rinsed with DI water and dried with air at room temperature.

Printing Architecture: The bottom-up printing setup consisted of a DLP-based projector PRO4500 from Wintech Digital System Technology Corporation, a motorized translation stage mounted to a motor controller and optical accessories from Thorlabs, Inc. The intrinsic resolution of the printer is $\approx 30 \mu\text{m}$.

Printing Procedure: All the printing proceeded in air under ambient conditions. Adequate amounts of the inks were then placed on the substrates. Then a designed pattern was projected onto the top surface of the transparent substrates. As the light irradiated on the substrate, the photoreduction reaction occurred and generate AuNPs at the irradiated sites. The projected pattern will be kept for a certain period of time to keep the reaction ongoing. After printing, the substrates with deposited gold were rinsed by ethanol and dried in air.

SEM Imaging and Processing: A scanning electron microscope was used to study the microstructures of the printed gold and measure the particle sizes and the porosity of the printed gold. The SEM images were obtained by using ZEISS Supra 40VP SEM. The as-printed samples were directly observed under SEM without further treatment. The obtained SEM images were smoothed, sharpened, and analyzed using the software ImageJ. The particle sizes were determined by measuring the longest length of the particles. To measure the porosity, the printed Au patterns were approximated as porous 2D films. SEM images were processed in ImageJ where a threshold tool was applied to obtain black and white images. Then specific areas were selected to measure area of pores and the mean pore area/selected area was calculated as the porosity.

Transmission and Reflectance Spectra: The transmission and reflectance spectra of the printed Au patterns were measured using USB2000+UV-VIS-ES spectrometer with a DH-2000-BAL UV-VIS-NIR light source from

Ocean Optics, Inc. The spectrometer was connected to a DM5000 B microscope from Leica Microsystems GmbH.

pH Value Measurement: The pH values of the precursor inks were measured using a FiveEasy Plus FP30 pH meter from Mettler-Toledo GmbH.

Thickness Measurement: The thickness of the printed gold patterns was measured with phase-shift interference (PSI) mode using a Bruker NT9300 optical profiler from Bruker Corporation.

Conductivity Measurement: The sheet resistances of the printed gold electrode were measured with a four-point probe tester from Suzhou Jingge Electronic Co., Ltd.

Resistance Stability Measurement: A rectangular gold pattern was printed on PDDA-coated PDMS thin film to measure its resistance stability under inward and outward bending and stretching. The resistance of the printed gold was measured using the 2450 digital multimeter from Keithley Instruments. A Cellscale Univert mechanical tester was used to conduct cyclic stretching on the samples. The resistance for long-term electrical stability of the printed gold was measured by an electrochemical workstation, CHI660E from CH Instrument. The data were recorded at the voltage of 0.1 V for 1 min for each test.

Electrochemical Impedance Measurement: Electrochemical impedance spectra (EIS) were measured by two-electrode configuration, where a pair of printed Au electrodes with an area of 2 mm \times 2 mm was used. Another pair of porous Au electrodes with same size for comparison was prepared by Pelco Auto Sputter Coater SC-7, Ted Pella Inc. PBS solution was used as the electrolyte for the tests. The electrochemical impedance spectra (EIS) were acquired by using an electrochemical workstation, CHI660E from CH Instrument. The data were recorded at the initial voltage of 0 V with an amplitude of 5 mV at the frequency in the range of 1–10⁴ Hz.

Electrical Stimulation and Measurement of the Flytrap: A pair of gold electrodes were printed on a PET substrate and (exposed areal of $\approx 5 \text{ mm}^2$) coated with a thin layer of poly(acrylic acid) (PAAc) hydrogel was attached to the lower epidermis of the flytrap lobe for electrical stimulation, which was applied by a square-wave alternating voltage ($\pm 3.0 \text{ V}$, frequency: 2 Hz) continuously. Another pair of printed gold electrodes coated with PAAc hydrogel was attached onto the other lobe of the same flytrap for measuring the action potential. The electrical signals were collected using the 2450 digital multimeter from Keithley Instruments.

Ex Vivo Ventricular Pacing: A pair of gold electrodes were printed on a PET substrate and coated with a thin layer of PAAc hydrogel as an adhesive layer. A postmortem study was performed in a male Yucatan miniature pig (S & S Farms, Ranchita, CA). All animal studies were approved by the UCLA Office of Animal Research in compliance with the UCLA IACUC protocols. The porcine epicardium was exposed through a thoracotomy, and the epicardium of the right ventricles was attached with printed gold electrodes. External pacing was conducted after euthanasia, with an amplitude of 2–3 V, a pulse width of 1 ms, and a pacing rate of 60 beats per minute.

ECG, EEG, and EMG Measurements: The electrocardiogram (ECG), electroencephalogram (EEG), and electromyogram (EMG) were measured and recorded using a Cyton + Daisy biosensing board (16 channels) connected with either the printed Au electrodes or commercial Ag/AgCl electrodes. A healthy volunteer was used as the human test subject. Ten20 conductive paste was applied evenly on the skin of the volunteer before attaching the conformal Au electrodes. No conductive paste was required for the Ag/AgCl electrodes due to the adhesive hydrogels inside. The software OpenBCI GUI was used to control the board to collect the data.

Study Approval: All experiments including the human testing and animal experiments were carried out in full compliance with local laws and ethical guidelines. Consent was obtained from the human subject involved in this study. Ethical approval for the experiments involving the human subjects was not required.

Statistical Analysis: All values of significance were determined using a one-way ANOVA with Microsoft Excel software. The sample size for

measuring the particles sizes equals to 80 for each recipe or condition analysis. The sample size for measuring thickness and porosity equals to 5 for each recipe or condition analysis. In Figure 5e,f, all raw data collected for ECG, EEG and EMG tests were filtered with a Butterworth filter using Python code (5–50 Hz for ECG and EMG signals, 7–13 Hz for EEG signals, with a notch at 60 Hz).

Supporting Information

Supporting Information is available from the Wiley Online Library or from the author.

Acknowledgements

The authors acknowledge the support of ONR award N000141712117, ONR award N00014-18-1-2314, AFOSR award FA9550-17-1-0311, AFOSR award FA9550-18-1-0449, AFOSR award FA9550-20-1-0344, NSF CAREER award 1724526, and start-up funds from the University of California, Los Angeles.

Conflict of Interest

The authors declare no conflict of interest.

Data Availability Statement

The data that support the findings of this study are available from the corresponding author upon reasonable request.

Keywords

conformable electrodes, gold patterning, photoreduction, projection lithography, specific ion effects

Received: February 23, 2022

Revised: April 11, 2022

Published online:

- [1] A. C. Fischer, F. Forsberg, M. Lapisa, S. J. Bleiker, G. Stemme, N. Roxhed, F. Niklaus, *Microsyst. Nanoeng.* **2015**, *1*, 15005.
- [2] D. Wang, Y. Zhang, X. Lu, Z. Ma, C. Xie, Z. Zheng, *Chem. Soc. Rev.* **2018**, *47*, 4611.
- [3] Y. Song, R. M. Panas, J. B. Hopkins, *Precis. Eng.* **2018**, *51*, 729.
- [4] P. Li, Y. Zhang, Z. Zheng, *Adv. Mater.* **2019**, *31*, 1902987.
- [5] A. M. Andrews, W. S. Liao, P. S. Weiss, *Acc. Chem. Res.* **2016**, *49*, 1449.
- [6] W. J. Sames, F. A. List, S. Pannala, R. R. Dehoff, S. S. Babu, *Int. Mater. Rev.* **2016**, *61*, 315.
- [7] D. J. Finn, M. Lotya, J. N. Coleman, *ACS Appl. Mater. Interfaces* **2015**, *7*, 9254.
- [8] Q. Huang, K. N. Al-Milaji, H. Zhao, *ACS Appl. Nano Mater.* **2018**, *1*, 4528.
- [9] J. Jiang, B. Bao, M. Li, J. Sun, C. Zhang, Y. Li, F. Li, X. Yao, Y. Song, *Adv. Mater.* **2016**, *28*, 1420.
- [10] M. Tavakoli, M. H. Malakooti, H. Paisana, Y. Ohm, D. Green Marques, P. Alhais Lopes, A. P. Piedade, A. T. de Almeida, C. Majidi, *Adv. Mater.* **2018**, *30*, 1801852.
- [11] K. N. Al-Milaji, Q. Huang, Z. Li, T. N. Ng, H. Zhao, *ACS Appl. Electron. Mater.* **2020**, *2*, 3289.
- [12] K. S. Bhat, U. T. Nakate, J. Y. Yoo, Y. Wang, T. Mahmoudi, Y. B. Hahn, *Chem. Eng. J.* **2019**, *373*, 355.
- [13] S. B. Walker, J. A. Lewis, *J. Am. Chem. Soc.* **2012**, *134*, 1419.
- [14] T. Tanaka, A. Ishikawa, S. Kawata, *Appl. Phys. Lett.* **2006**, *88*, 081107.
- [15] A. Ishikawa, T. Tanaka, S. Kawata, *Appl. Phys. Lett.* **2006**, *89*, 113102.
- [16] Y. Liu, Q. Hu, F. Zhang, C. Tuck, D. Irvine, R. Hague, Y. He, M. Simonelli, G. A. Rance, E. F. Smith, R. D. Wildman, *Polymers* **2016**, *8*, 325.
- [17] E. Blasco, J. Müller, P. Müller, V. Trouillet, M. Schön, T. Scherer, C. Barner-Kowollik, M. Wegener, *Adv. Mater.* **2016**, *28*, 3592.
- [18] B. B. Xu, Z. C. Ma, L. Wang, R. Zhang, L. G. Niu, Z. Yang, Y. L. Zhang, W. H. Zheng, B. Zhao, Y. Xu, Q. D. Chen, H. Xia, H. B. Sun, *Lab Chip* **2011**, *11*, 3347.
- [19] Z.-C. Ma, Y.-L. Zhang, B. Han, Q.-D. Chen, H.-B. Sun, *Small Methods* **2018**, *2*, 1700413.
- [20] Q. Ge, Z. Li, Z. Wang, K. Kowsari, W. Zhang, X. He, J. Zhou, N. X. Fang, *Int. J. Extreme Manuf.* **2020**, *2*, 022004.
- [21] D. Wu, J. Song, Z. Zhai, M. Hua, C. Kim, I. Frenkel, H. Jiang, X. He, *ACS Appl. Mater. Interfaces* **2019**, *11*, 47468.
- [22] M. Hua, D. Wu, S. Wu, Y. Ma, Y. Alsaied, X. He, *ACS Appl. Mater. Interfaces* **2021**, *13*, 12689.
- [23] M. Gregorini, R. N. Grass, W. J. Stark, *Ind. Eng. Chem. Res.* **2020**, *59*, 12048.
- [24] Y. Zhang, Z. Liang, A. P. Zhang, H. Tam, *Adv. Opt. Mater.* **2021**, *9*, 2001368.
- [25] X. Yang, M. Sun, Y. Bian, X. He, *Adv. Funct. Mater.* **2019**, *29*, 1807615.
- [26] X. Wang, K. Cui, Q. Xuan, C. Zhu, N. Zhao, J. Xu, *ACS Appl. Mater. Interfaces* **2019**, *11*, 21668.
- [27] X. Liu, X. Zhou, Y. Li, Z. Zheng, *Chem. – Asian J.* **2012**, *7*, 862.
- [28] Z. Zhao, J. Bai, Y. Yao, C. Wang, *Mater. Today* **2020**, *37*, 10.
- [29] M. Hua, S. Wu, Y. Ma, Y. Zhao, Z. Chen, I. Frenkel, J. Strzalka, H. Zhou, X. Zhu, X. He, *Nature* **2021**, *590*, 594.
- [30] S. Wu, M. Hua, Y. Alsaied, Y. Du, Y. Ma, Y. Zhao, C. Y. Lo, C. Wang, D. Wu, B. Yao, J. Strzalka, H. Zhou, X. Zhu, X. He, *Adv. Mater.* **2021**, *33*, 2007829.
- [31] Z. He, W. J. Xie, Z. Liu, G. Liu, Z. Wang, Y. Q. Gao, J. Wang, *Sci. Adv.* **2016**, *2*, e1600345.
- [32] V. Merk, C. Rehbock, F. Becker, U. Hagemann, H. Nienhaus, S. Barcikowski, *Langmuir* **2014**, *30*, 4213.
- [33] R. Du, Y. Hu, R. Hübner, J. O. Joswig, X. Fan, K. Schneider, A. Eychmüller, *Sci. Adv.* **2019**, *5*, eaaw4590.
- [34] P. Bianchi, G. Petit, J. C. M. Monbaliu, *React. Chem. Eng.* **2020**, *5*, 1224.
- [35] C. Fan, T. Bian, L. Shang, R. Shi, L. Z. Wu, C. H. Tung, T. Zhang, *Nanoscale* **2016**, *8*, 3923.
- [36] J. He, Y. Wang, Y. Feng, X. Qi, Z. Zeng, Q. Liu, W. S. Teo, C. L. Gan, H. Zhang, H. Chen, *ACS Nano* **2013**, *7*, 2733.
- [37] Q. Cheng, L. Song, H. Lin, Y. Yang, Y. Huang, F. Su, T. Chen, *Langmuir* **2020**, *36*, 250.
- [38] W. Li, N. Matsuhisa, Z. Liu, M. Wang, Y. Luo, P. Cai, G. Chen, F. Zhang, C. Li, Z. Liu, Z. Lv, W. Zhang, X. Chen, *Nat. Electron.* **2021**, *4*, 134.